A distance regularized level-set evolution model based MRI dataset segmentation of brain's caudate nucleus

It is advisable to refer to the publisher's version if you intend to cite from the work. See Guidance on citing.

To link to this article DOI: http://dx.doi.org/10.1109/ACCESS.2019.2937964

www.reading.ac.uk/centaur

CentAUR

Central Archive at the University of Reading

Reading's research outputs online

A Distance Regularized Level-Set Evolution Model Based MRI Dataset Segmentation of Brain's Caudate Nucleus

YATING CHEN[1], GAOXIANG CHEN[1], YU WANG[1], NILANJAN DEY[2], R. SIMON SHERRATT[3], (Fellow, IEEE), AND FUQIAN SHI[1], (Senior Member, IEEE)

[1]First Affiliated Hospital of Wenzhou Medical University, Wenzhou 325035, China
[2]Department of Information Technology, Techno India College of Technology, Kolkata 700156, India
[3]Department of Biomedical Engineering, University of Reading, Reading RG6 6AY, U.K.

Corresponding author: Fuqian Shi (sfq@wmu.edu.cn)

ABSTRACT The caudate nucleus of the brain is highly correlated to the emotional decision-making of pessimism, which is an important process for improving the understanding and treatment of depression; and the segmentation of the caudate nucleus is the most basic step in the process of analysis and research concerning this region. In this paper, Level Set Method (LSM) is applied for caudate nucleus segmentation. Firstly, Distance Regularized Level Set Evolution (DRLSE), Region-Scalable Fitting (RSF) and Local Image Fitting (LIF) models are proposed for segmentation of the caudate nucleus of Magnetic Resonance Imaging (MRI) images of the brain, and the segmentation results are compared by using selected evaluation indices. The average Dice Similarity Coefficient (DSC) values of the proposed three methods all exceed 85%, and the average Jaccard Similarity (JS) values are over 77%, respectively. The results indicate that all these three models can have good segmentation results for medical images with intensity inhomogeneity and meet the general segmentation requirements, while the proposed DRLSE model performs better in segmentation.

INDEX TERMS Distance regularized level set evolution, local image fitting, level set method, medical image segmentation, region-scalable fitting.

I. INTRODUCTION

With the development of science and technology, advanced brain imaging technologies and new types of equipment are constantly appearing. The existing brain imaging technologies include Magnetic Resonance Imaging (MRI), Positron Emission Computed Tomography (PET), Electroencephalography (EEG), Magnetoencephalography (MEG), Computed Tomography (CT), Single-Photon Emission Computed Tomography (SPECT), Diffusion Tensor Imaging (DTI), etc. These brain imaging techniques have become an indispensable means to carry out disease diagnosis, surgical planning, and prognosis assessment. And, in the process of analysis of medical images obtained by these imaging techniques, medical image processing is the first step which helps researchers to improve the readability of medical images

and the efficiency of diagnosis. Therefore, medical image processing has been attached great importance globally. Image segmentation is not only the basis of image processing, but also a key point and a difficult point, which is the bottleneck of restricting the application of three-dimensional (3D) reconstruction technology. The value of medical image segmentation is mainly reflected in the following two aspects: a) The human tissues and organs or lesion tissues can be extracted by medical image segmentation to assist in the diagnosis, treatment planning, and clinical research. It saves time and effectively reduces the diagnostic errors. b) It is convenient to perform real-time 3D reconstruction and visualization. 3D reconstruction is computationally expensive and time-consuming, but the requirements for real-time 3D reconstruction are high in clinical medicine. The original image is compressed after being segmented, which reduces the computational complexity and makes the image satisfy the real-time and precision in 3D reconstruction.

The associate editor coordinating the review of this article and approving it for publication was Sunil Karamchandani.

Traditional medical image segmentation is where a health care professional completes the identification work by manual segmentation according to the actual situation of the target location or actual anatomical structure. Although the result of manual segmentation is the most reliable, the amount of image data is so large that the workload of the image analysis and segmentation is large, and such workload requires a reliable semi-automatic or automatic segmentation scheme to complete to save time. With the development of computer image processing technology, some traditional image processing methods have been widely used in medical image segmentation, and new segmentation methods are constantly emerging. Among them, the level set method can handle topological changes, such as splitting and merging, in a natural and efficient way, and can flexibly combine energy terms, which not only can segment ordinary images, but also has a good segmentation effect on complex images. Therefore, this has been the focus of research in recent years. The Region-Scalable Fitting (RSF) model is a region-based active contour model proposed by Li *et al.* [1], which was originally called Local Binary Fitting (LBF) model [2]. By adjusting the difference between the level set function and the signed distance function, this model ensures the accurate calculation and avoids re-initialization of the evolution process. The Local Image Fitting (LIF) model [3] was developed from the LBF model, being a novel active contour model driven by local image fitting energy. The model uses a Gaussian kernel instead of the traditional regularized term to regulate the level set function and has a good segmentation effect and high computational efficiency. Li *et al.* [4] put forward a Distance Regularized Level Set Evolution (DRLSE) model, which eliminated the need for re-initialization and guaranteed the evolutionary stability. They also applied DRLSE to the edge-based active contour model for image segmentation and achieved good results. Later, researchers combined and improved these models and obtained many new practical medical image segmentation methods. Bhadauria and Dewal [5] presented an active contour model for hemorrhage detection in brain CT images which combined the spatial Fuzzy C-Mean (FCM) algorithm and the RSF model. The purpose of this combination was to apply the results of FCM clustering to the initial contour of RSF model. Ding *et al.* [6] segmented images with intensity inhomogeneity by another active contour model that integrated the region-scalable fitting energy with an optimized Laplace Gaussian (LoG) energy. The proposed model overcame the problem of sensitivity to initial contour and achieved higher segmentation accuracy and efficiency relative to other region-based models. Wang *et al.* [7] based on LBF and LIF models, constructed a fitting energy of a local mixed image to obtain a new active contour model, which had better results than available region-based models in terms of accuracy and effectiveness. Wang *et al.* [8] proposed a new region-based active contour model with a Hybrid Region Image Fitting (HRIF) energy function. This energy function was defined using two different local fitted images.

One was an Extended Fitted Image (EFI), being an expansion form of the Local Fitted Image (LFI) [3] and another is a Square Fitted Image (SFI). Sethi *et al.* [9] defined a novel level set method for segmenting low contrast cancerous regions in CT images, including regional separation, region enhancement, and DRLSE with a new stopping function. Results showed the superiority of the proposed method on 2D and 3D CT images. Liu *et al.* [10] extended the edge-based DRLSE model to a two-level set formulation and applied it to the segmentation of left and right ventricles from cine-MRI images, which had some effect. Zhang *et al.* [11] proposed a two-step segmentation method based on DRLSE for prostate MRI which achieved the segmentation of the central prostate and the periphery of the prostate. They used the multi-line segment fitting method to initialize the level set function, which prompted the segmentation algorithm to have improved boundary converge. However, it was unable to meet the segmentation requirements of multi-regional conditions in different scanning layers of prostate MRI. Gautam *et al.* [12] presented a hybrid method for segmentation of brain lesion regions in CT images of hemorrhagic lesion, which combined fuzzy clustering using a hyper tangent function and the DRLSE function to obtain the smooth boundary of the segmented regions with high segmentation accuracy. Wu *et al.* [13] proposed a robust and stable automatic heart motion tracking method. A heart shape model was established by training a three-layered deep Boltzmann machine (DBM) and then embedded into the DRLSE method as a shape prior term to constrain an evolutional shape to delineate the heart contour on each frame of a cine MRI image sequence. These excellent methods have enabled more accurate and efficient medical image segmentation, and made significant contributions to clinical research, disease diagnosis and classification.

Previous studies indicated that depression, Alzheimer's Disease (AD), and schizophrenia have been the most common diseases while are great impact on social and economic development. However, according to the existing medical image segmentation research, the caudate nucleus segmentation is seldom involved. The improved level set method to segment the caudate nucleus is effective. It can perform dimensionality reduction on the original MR image, help to improve the readability of medical images, and improve analysis efficiency. Our research will play an important contribution to the clinical research, disease diagnosis and classification of mental disorders such as AD and depression. How to detect [14], delay, treat, and predict [15] brain dysfunction has become the emphasis of medical researchers. Al-shaikhli *et al.* [16] proposed an automatic 3D caudate nucleus segmentation and an AD detection method based on coupled dictionary learning with a level set formulation. The segmentation and classification accuracy rates were found to be 91.5% and 92.5%, respectively. In addition, they believed that the study of caudate nucleus atrophy was helpful for the detection of AD than the study of atrophy of whole brain structure. In terms of depression, a recent study by
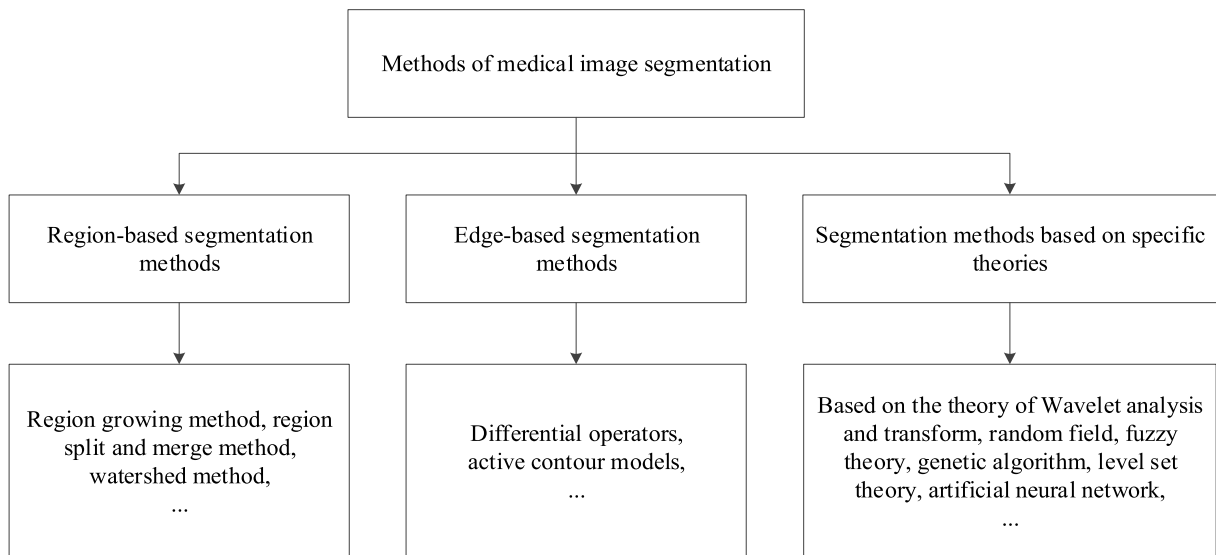
FIGURE 1. Methods of medical image segmentation.

Ken-Ichi *et al.* [17] showed that negative reactions occur when stimulating the caudate nucleus of an animal brain, thus proving that the region of caudate nucleus is mainly responsible for emotional decision-making of pessimistic emotions. This study is expected to help scientists better understand and treat depression. For the research work in this field, the most basic and necessary requirement is the segmentation of caudate nucleus. By segmenting the caudate nucleus, researchers can observe the area more intuitively and clearly. Research on a dimension-reduced image [18] after segmentation can simplify the calculation and improve the efficiency of analysis. In this paper, a semi-automatic interaction method is used to form an initial contour frame. The parameter settings according to the existing MR image dataset was adjusted, and effectively improved the segmentation rate of the caudate nucleus. The RSF, LIF, and DRLSE models were selected for segmentation and the results indicated that the proposed DRLSE model has the best segmentation ability by comparing with ground truth image dataset. The parameters setting and feature calculation in this research are novelty and the proposed model for MRI of caudate nucleus is feasible and effective.

The rest of this paper is organized as follows: In Section 2, the principle of the level set method and three level set models are introduced. Then, in Section 3, we give a detailed description of our simulation experiment setup. Results and discussion are made in Section 4. Finally, concluding remarks and future work are discussed in Section 5.

II. METHODS OF MEDICAL IMAGE SEGMENTATION
A. METHODS OF MEDICAL IMAGE SEGMENTATION
Image segmentation is a fundamental, but critical step in medical image processing. It is an important basis and premise for understanding many medical problems. Accurate medical image segmentation results can provide the necessary basic data for the diagnosis and treatment of diseases and the formulation of clinical treatment prescription. On one hand, the medical image has the characteristics of particularity, complexity, and partial volume effect. At the same time, it is susceptible to various external factors such as equipment performance, subject movement, noise, and bias field, which makes the actual medical images mostly have the features of fuzziness and inhomogeneity. On the other hand, the complexity and irregularity of the organ structure cause great differences in medical images. Because of the above reasons, medical image segmentation is still one of the major problems to be solved.

Image segmentation is the process of dividing an image into regions of interest, which can then be further analyzed and understood. Based on the inherent features of the image, such as grayscale, color, texture, contrast, local statistical features, and spectral characteristics, the image is divided into homogeneous regions with their respective characteristics. With the rapid improvement of health care, the research and development of medical image segmentation technologies have been widely concerned and many new methods of medical image segmentation have emerged. Although there are many methods for segmenting medical images, most of them are based on different segmentation tasks or different imaging technologies. These methods are generally highly targeted, and there is no uniform standard to solve all the segmentation problems. Typical medical image segmentation methods in the medical field can be summarized as follows: region-based segmentation methods, edge-based segmentation methods, and segmentation methods based on specific theories, with some of the most important methods given in Fig. 1. (1) The region-based segmentation method divides an image into different sub-regions according to similarity measures of certain features in different regions. It mainly includes region growing method, region split and merge method,

and watershed method. (2) The edge-based segmentation method usually detects the edges between regions to achieve segmentation by using the discontinuity of pixel degrees between different regions. It includes differential operators and active contour models. (3) Segmentation method is based on specific theories - with the rapid development of computer vision and artificial intelligence, new research findings are being introduced into medical image segmentation. The common methods include: multi-scale segmentation technology based on wavelet analysis and transform, segmentation technology based on random field theory [19], segmentation technology based on fuzzy theory [20], segmentation technology based on genetic algorithm [21], [22], segmentation technology based on level set theory, segmentation technology based on artificial neural networks [23], [24].

B. LEVEL SET METHOD

The level set method has mainly been developed from the field of interface propagation and is a numerical technique for interface tracking and shape modeling. In 1988, Osher and Sethian [25] first proposed the concept of the level set, which was mainly used to solve the shape change process of flames following the thermodynamic equation. Due to the high dynamics of the flame shape and the uncertainty of the topology, it is hard to describe the change of the flame shape in traditional parametric form. For this reason, they proposed a concept of level set to describe the time-dependent motion interface.

The core operation of the level set method is to express a two-dimensional curve implicitly as the zero-level set of a three-dimensional continuous function surface. By constantly updating the level set function, the zero-level set is changed to achieve the continuous evolution of the curve. It can be said that its essence is to solve a partial differential equation. An important theoretical premise of this method is the concept of the implicit function. The purpose of introducing the level set concept into the curve evolution theory was to provide an implicit expression for the curve, thereby avoiding a series of problems caused by the explicit expression of the parameterization. The implicit expression has obvious advantages in describing curvilinear motion. For example, when several curves merge into one curve in motion, or a curve splits into several curves, such a topology change cannot be expressed by the motion of a continuous parametric curve. However, the topological change of the above curve can be expressed as the change of the intersecting lines of a continuously changing surface and a fixed plane, such as a plane with zero z axis, which makes the complex curve motion process transform into a process of the higher dimensional function evolution. If the level set function remains as a valid function, the curve which is implicit in the function can be changed in any topology. This is a good solution to the problem that the parameterization method cannot satisfy topology changes. Therefore, compared with the traditional image segmentation method, the level set method has significant advantages: The implicitly expressed evolution curve

(or surface) can naturally change its topology, so that the objects with complex shapes can be segmented in the image. It can avoid tracking the evolution process of the closed curve (or surface) and transform the evolution of curve (or surface) into a numerical solution of partial differential equation. It can also be easily extended to high-dimensional cases supported by its strong theoretical background. Because of these advantages, the level set method has a wide range of uses in medicine, mechanics of materials, hydrodynamics, computer vision, amongst others.

A closed curve on a two-dimensional plane is defined as $y = f(x)$, or is written as $y - f(x) = 0$. If we assume that $\phi(x, y) = y - f(x)$, then, $\phi(x, y) = 0$ is the implicit expression of the curve $y = f(x)$. The law of the evolution of the level set can be further analyzed. If a function $\phi(C, t)$ is a set, then the zero-level set corresponding to the curve $C(t)$ at time t is:

$$\phi(C(t), t) = 0. \tag{1}$$

The partial derivative of the above formula is:

$$\frac{\partial \phi}{\partial t} + \nabla \phi \cdot \frac{\partial C}{\partial t} = 0, \tag{2}$$

where, $\nabla \phi$ is the gradient of ϕ. Let the arc length parameter of C be s. From the curve evolution theory and the level set concept, the variation of ϕ along the tangent of C is $\partial \phi / \partial s = 0$, that is:

$$0 = \frac{\partial \phi}{\partial x} \frac{\partial x}{\partial s} + \frac{\partial \phi}{\partial y} \frac{\partial y}{\partial s} = \langle \nabla \phi, \frac{\partial C}{\partial s} \rangle. \tag{3}$$

$\nabla \phi$ is perpendicular to the tangent $\partial C / \partial s$, which is in line with the normal direction. If ϕ is specified to be a negative value inside the zero-level set and a positive value outside the zero level set, the unit normal vector of the level set curve is:

$$\vec{N} = -\frac{\nabla \phi}{|\nabla \phi|}. \tag{4}$$

and the curve evolution equation is often defined as:

$$\frac{\partial C}{\partial t} = F\vec{N}, \tag{5}$$

where, F is the velocity function of the curve. Finally, the equation of the curve evolution expressed by the level set function can be got through combining equations (2), (4), and (5), shown as follows:

$$\frac{\partial \phi}{\partial t} = -\nabla \phi \cdot \frac{\partial C}{\partial t} = -\nabla \phi \cdot F \cdot \vec{N} = F |\nabla \phi|. \tag{6}$$

In conclusion, the level set method is a process of transforming the evolution of the closed curve into the evolution of the level set function, and then solving the corresponding partial differential equation.

C. CLASSIFICATION OF LEVEL SET MODELS

Level set models are mainly divided into two categories: edge-based level set models and region-based level set models.

1) EDGE-BASED LEVEL SET MODELS

Such models use local edge information to make the evolution curve approximate to the target contour. So, they are more suitable for segmenting images with strong edges. However, because this kind of model relies too much on the gradient information of the target edge, its approximation effect is not ideal for images with edges with no obvious gradient changes. The evolution curve often crosses the edge and leads to poor segmentation effect. The most famous edge-based level set model is the Snake model proposed by Kass *et al.* [26]. Its main principle is to set the edge function for the initial contour of the target, and then the driving force drives the initial contour curve to contract toward the maximum gradient. When the function gets the minimum extreme value, the final segmentation result is obtained. The defect of this model is that it is sensitive to the initial contour position and may plunge into local optima. It has almost no convergence in the concave area. For the problem that it is not easy to detect the edge of the depression area, the Gradient Vector Flow (GVF) model has been proposed [27], which can detect the concave boundary of the target well by means of gradient vector flow instead of the traditional external force field. The DRLSE model proposed by Li *et al.* [4] is a very practical edge-based level set model.

2) REGION-BASED LEVEL SET MODELS

The region-based level set models are usually segmented images by constraints such as contour curvature and area of the target region. The most typical one is the C-V model [28]. However, it assumes that the image grayscale is homogeneous distributed in each region. So, it is hard to segment medical images with weak contrast and uneven brightness. Also, this model is time-consuming due to constantly initialize the function. Both RSF models proposed by Li *et al.* [1] and LIF model proposed by Zhang *et al.* [3] belong to region-based level set models.

D. ALGORITHM OF LEVEL SET MODELS

The following is a brief introduction to three kinds of level set models, namely RSF model, LIF model, and DRLSE model. Then the simulation experiments will be carried out on this basis.

1) REGION-SCALABLE FITTING (RSF) MODEL

This section introduces the RSF) model [1]. Firstly, a region-scalable fitting energy functional consisting of a contour and two fitting functions is defined. The best fitting functions are used to extract the average of the local grayscale on both sides of the contour as the local region information to construct the energy function. Since the kernel function has scale parameters, the region-scalable fitting energy can use the region grayscale information from the small region to the whole region within a controllable range, thus driving the contour to the target boundary. Therefore, this model can be used to segment the image with gray inhomogeneity.

The region-scalable fitting energy is merged into a variational level set formulation with a regularization term, from which a curve evolution equation for energy minimization is exported. This model can avoid the reinitialization of the level set function and improve the operation speed. The model is defined as:

$$\frac{\partial \phi}{\partial t} = -\delta_\epsilon(\phi)(\lambda_1 e_1 - \lambda_2 e_2) + \nu\delta_\epsilon(\phi)\,\mathrm{div}\left(\frac{\nabla\phi}{|\nabla\phi|}\right) + \mu\left(\nabla^2\phi - \mathrm{div}\left(\frac{\nabla\phi}{|\nabla\phi|}\right)\right). \quad (7)$$

The first term on the right side is referred to as the region-scalable fitting energy term which is responsible for driving the active contour toward object boundaries. The region-scalable property of the fitting energy can be represented by changing the size of parameter σ. The second term has a shortening or smoothing effect on the zero-level contour, hence it is called the arc length term. The last term is the regularization term, since it is used to maintain the regularity of the level set function. ∇ is the Laplacian operator and div() is the divergence operator. λ_1, λ_2, ν, and μ are constants which can be modified according to the actual image. The function H_ϵ is a smoothing function in this model, which usually used to approximate the Heaviside function:

$$H_\epsilon(x) = \frac{1}{2}\left[1 + \frac{2}{\pi}arctan\left(\frac{x}{\epsilon}\right)\right]. \quad (8)$$

The derivative of H_ϵ is

$$\delta_\epsilon(x) = H_\epsilon'(x) = \frac{1}{\pi}\frac{\epsilon}{\epsilon^2 + x^2}. \quad (9)$$

e_1 and e_2 are defined as follows:

$$e_i(\mathrm{x}) = \int K_\sigma(\mathrm{y} - \mathrm{x})\,|I(\mathrm{x}) - f_i(\mathrm{y})|^2\,dy, \quad i = 1, 2. \quad (10)$$

The kernel function K is chosen as a Gaussian kernel:

$$K_\sigma(\mathrm{u}) = \frac{1}{(2\pi)^{n/2\sigma^n}}e^{-|\mathrm{u}|^2/2\sigma^2} \quad (11)$$

with a scale parameter $\sigma > 0$. Also:

$$f_i(\mathrm{x}) = \frac{K_\sigma(\mathrm{x}) * \left[M_i^\epsilon(\phi(\mathrm{x}))\,I(\mathrm{x})\right]}{K_\sigma(\mathrm{x}) * M_i^\epsilon(\phi(\mathrm{x}))}, \quad i = 1, 2. \quad (12)$$

where $M_1^\epsilon(\phi) = H_\epsilon(\phi) > 0$ and $M_2^\epsilon(\phi) = 1 - H_\epsilon(\phi) > 0$. So f_2 in (12) can also be written as:

$$f_2 = \frac{K_\sigma * I - K_\sigma * [H_\epsilon(\phi)\,I]}{K_\sigma * 1 - K_\sigma * H_\epsilon(\phi)}. \quad (13)$$

Algorithm 1 is the pseudocode of the RSF algorithm.

2) LOCAL IMAGE FITTING (LIF) MODEL

By considering the RSF model, Zhang *et al.* [3] proposed a novel active contour model driven by local image fitting energy. They replaced the local intensity fitting energy in the RSF algorithm with the local image fitting energy, and then obtained the local image fitting energy function by minimizing the difference between the fitted image and the

---

Algorithm 1 Region-Scalable Fitting (RSF)

INPUT: u0, Img, Ksigma, KI, KONE, nu, timestep, mu, lambda1, lambda2, epsilon, numIter

OUTPUT: u

1. $u \leftarrow u0$;

2. **FOR** k1 = 1 to numIter **DO**

3. Update u according to Neumann boundary condition and initial function u0;

4. Calculate the mean curvature of the level contours of the function u, that is div (u) ;

5. Calculate $\delta_\epsilon (u)$ using $\delta_\epsilon (u) = H_\epsilon^{'} (u) = \frac{1}{\pi} \frac{\epsilon}{\epsilon^2 + u^2}$;

6. Obtain the fitting value f_1 and f_2 according to $f_1 = \frac{K_\sigma * [H_\epsilon (u) I]}{K_\sigma * H_\epsilon (u)}$ and $f_2 = \frac{K_\sigma * I - K_\sigma * [H_\epsilon (u) I]}{K_\sigma * 1 - K_\sigma * H_\epsilon (u)}$;

7. Plug $e_i (x) = \int K_\sigma (y - x) |I (x) - f_i (y)|^2 \, dy, i = 1, 2$ into $(\lambda_1 e_1 - \lambda_2 e_2)$ and calculate $(\lambda_1 e_1 - \lambda_2 e_2)$;

8. Update u according to
$$\frac{\partial \phi}{\partial t} = -\delta_\epsilon (\phi) (\lambda_1 e_1 - \lambda_2 e_2) + \nu \delta_\epsilon (\phi) \text{div} \left(\frac{\nabla \phi}{|\nabla \phi|} \right) + \mu \left(\nabla^2 \phi - \text{div} \left(\frac{\nabla \phi}{|\nabla \phi|} \right) \right);$$

9. **END FOR**

Algorithm 2 Local Image Fitting (LIF)

INPUT: I, phi, timestep, epsilon, K

OUTPUT: phi

1. Make phi satisfy Newman boundary condition;

2. Calculate $H_\varepsilon (\phi)$ according to $H_\epsilon (x) = \frac{1}{2} \left[1 + \frac{2}{\pi} arctan \left(\frac{x}{\epsilon} \right) \right]$;

3. Calculate $\delta_\varepsilon (\phi)$ according to $\delta_\epsilon (x) = H_\epsilon^{'} (x) = \frac{1}{\pi} \frac{\epsilon}{\epsilon^2 + x^2}$;

4. Calculate m_1 and m_2 according to $m_1 = \frac{K_\sigma * [H_\epsilon (x) I]}{K_\sigma * H_\epsilon (x)}$ and $m_2 = \frac{K_\sigma * I - K_\sigma * [H_\epsilon (x) I]}{K_\sigma * 1 - K_\sigma * H_\epsilon (x)}$;

5. Update phi according to
$$\frac{\partial \phi}{\partial t} = ((I - m_1 H_\varepsilon (\phi)) - m_2 (1 - H_\varepsilon (\phi))) (m_1 - m_2) \delta_\varepsilon (\phi).$$

---

original image. They used a Gaussian kernel instead of the traditional regularized term to regularize the level set function, so the model can also be named the Gaussian regularized level set model. This model can not only acquire a similar segmentation results to the LBF energy model, but also maintain the sub-pixel accuracy and boundary regularization properties. The most important point is that it is much more computationally efficient.

Zhang defined a local fitted image (LFI) formulation as:

$$I^{\text{LFI}} = m_1 H_\varepsilon (\phi) + m_2 (1 - H_\varepsilon (\phi)) \tag{14}$$

where m_1 and m_2 are defined as follows:

$$\begin{cases} m_1 = \text{mean} (I \in (\{x \in \Omega \,|\, \phi (x) < 0\} \cap W_k (x))) \\ m_2 = \text{mean} (I \in (\{x \in \Omega \,|\, \phi (x) > 0\} \cap W_k (x))). \end{cases} \tag{15}$$

where, $W_k (x)$ is a rectangular window function such as a truncated Gaussian window function or a constant window function. Then a local image fitting energy functional is:

$$E^{\text{LFI}} (\phi) = \frac{1}{2} \int \left| I (x) - I^{\text{LFI}} (x) \right|^2 dx, \quad x \in \Omega. \tag{16}$$

Finally, Zhang minimized $E^{\text{LFI}} (\phi)$ with respect to ϕ to get the corresponding gradient descent flow:

$$\frac{\partial \phi}{\partial t} = \left(I - I^{\text{LFI}} \right) (m_1 - m_2) \delta_\varepsilon (\phi) = ((I - m_1 H_\varepsilon (\phi)) - m_2 (1 - H_\varepsilon (\phi))) (m_1 - m_2) \delta_\varepsilon (\phi). \tag{17}$$

The $H_\varepsilon (x)$ and $\delta_\varepsilon (x)$ terms in the above formula can be found from (8) and (9). The computation of m_1 and m_2 is the same as (12).

Algorithm 2 is the pseudocode of the LIF algorithm.

3) DISTANCE REGULARIZED LEVEL SET EVOLUTION (DRLSE) MODEL

Li *et al.* [4] proposed an improved variational level set formulation based on the traditional edge-based level set segmentation algorithms. They proposed a new energy term called a distance regularization term to constrain the level set function to remain stable throughout the iterative process. It effectively overcomes the problem that the traditional level set algorithm needs to reinitialize the level set function during the iterative process and improves the segmentation speed. At the same time, the distance regular term proposed by this algorithm can be transplanted into another level set algorithm models and achieve good results.

$$\frac{\partial \phi}{\partial t} = \mu \text{div} \left(d_p (|\nabla \phi|) \nabla \phi \right) - \frac{\partial \varepsilon_{ext}}{\partial \phi} \tag{18}$$

$$\frac{\partial \phi}{\partial t} = \mu \text{div} \left(d_p (|\nabla \phi|) \nabla \phi \right) + \lambda \delta_\varepsilon (\phi) \text{div} \left(g \frac{\nabla \phi}{|\nabla \phi|} \right) + \alpha g \delta_\varepsilon (\phi) \tag{19}$$

Equation (18) is a general form of DRLSE. Equation (19) is the form when DRLSE is applied to an edge-based active contour model. The first term on the right side in eqn. (19) is called the distance regularization term which is associated with the potential function, while the second and third terms are associated with the weighted length term and the weighted area term. μ is a constant, div() is the divergence operator and d_p is defined by:

$$d_p (s) \triangleq \frac{p^{'} (s)}{s} \tag{20}$$

where, p is a potential function for distance regularization. A simple and straightforward definition of the single-well potential p_1 is:

$$p = p_1 (s) \triangleq \frac{1}{2} (s - 1)^2 \tag{21}$$

It should be noted that the double-well potential p_2 is a better potential function for the distance regularization as

follows:

$$p_2(s) = \begin{cases} \dfrac{1}{(2\pi)^2} \left(1 - \cos(2\pi s)\right), & \text{if } s \leq 1 \\ \dfrac{1}{2}(s-1)^2, & \text{if } s \geq 1 \end{cases} \quad (22)$$

The first and second derivatives of p_2 are given by:

$$p_2'(s) = \begin{cases} \dfrac{1}{2\pi} \sin(2\pi s), & \text{if } s \leq 1 \\ s-1, & \text{if } s \geq 1 \end{cases} \quad (23)$$

and:

$$p_2''(s) = \begin{cases} \cos(2\pi s), & \text{if } s \leq 1 \\ 1, & \text{if } s \geq 1 \end{cases} \quad (24)$$

The function $d_p(s) = p_2'(s)\big/ s$ satisfies:

$$\left| d_p(s) \right| < 1, \quad \text{for all } s \in (0, \infty) \quad (25)$$

and:

$$\lim_{s \to 0} d_p(s) = \lim_{s \to \infty} d_p(s) = 1 \quad (26)$$

In addition, $\lambda > 0$ and $\alpha \in R$ are the coefficients of the edge term and area term. And g is an edge indicator function as:

$$g \triangleq \frac{1}{1 + |\nabla G_\sigma * I|^2} \quad (27)$$

where G_σ is a Gaussian kernel with a standard deviation σ, and I is an image on a domain Ω. According to Li *et al.* [4], δ_ε is defined by:

$$\delta_\varepsilon(x) = \begin{cases} \dfrac{1}{2\varepsilon}\left[1 + \cos\left(\dfrac{\pi x}{\varepsilon}\right)\right], & |x| \leq \varepsilon \\ 0, & |x| > \varepsilon \end{cases} \quad (28)$$

Algorithm 3 is the pseudocode of the DRLSE algorithm.

III. EXPERIMENTAL DESIGN
A. DATA PREPARATION
The data set used in the experiment is from Openneuro.[1] The file format downloaded from the public MRI dataset is ".nii", which contains images and image information. The scanned structure image (T1-weighted FLASH (Fast Low Angle Shot), TR (Time of Repetition) = 12 ms; TE (Time of Echo) = 5.6 ms; 1 mm³ resolution) [29] obtained from the dataset have been pretreated with skull stripping. Then these files are read through the NIFTI toolkit in MATLAB and eighteen axial slices are pick out and saved as JPG images for the experiment of caudate nucleus segmentation. Fig. 2 shows all of the original images.

B. THE FLOW CHART OF THE EXPERIMENT
The experimental procedures of the three models are essentially the same, divided into five steps. Fig. 3 presents the flow chart of the experiment.

[1]https://openneuro.org

Algorithm 3 Distance Regularized Level Set Evolution (DRLSE)

INPUT: phi_0, g, lambda, mu, alpha, epsilon, timestep, iter, potentialFunction
OUTPUT: phi
1. Construct g according to $g \triangleq \frac{1}{1+|\nabla G_\sigma * I|^2}$;
2. phi ← phi_0;
3. **FOR** k = 1 to iter **DO**
4. Update phi according to Neumann boundary condition and initial function phi_0;
5. Calculate the curvature of phi;
6. **IF** potentialFunction = 'single-well' **THEN**
7. Calculate p_1' according to $p_1'(s) = (s-1)$;
8. **ELSEIF** potentialFunction = 'double-well' **THEN**
9. Calculate p_2' according to
$$p_2'(s) = \begin{cases} \frac{1}{2\pi}\sin(2\pi s), & \text{if } s \leq 1 \\ s-1, & \text{if } s \geq 1; \end{cases}$$
10. **ELSE**
11. error
12. **END IF**
13. Update phi according to
$\frac{\partial \phi}{\partial t} = \mu \operatorname{div}\left(d_p(|\nabla \phi|)\nabla \phi\right) + \lambda \delta_\varepsilon(\phi)\operatorname{div}\left(g\frac{\nabla\phi}{|\nabla\phi|}\right) + \alpha g \delta_\varepsilon(\phi)$;
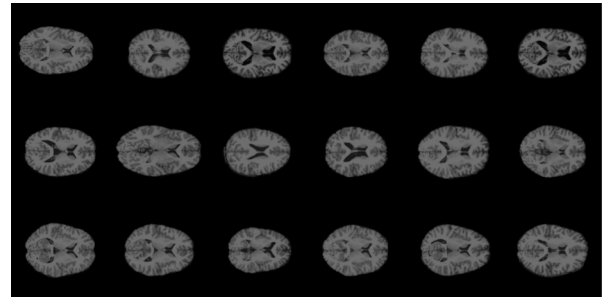14. **END FOR**

FIGURE 2. T1-weighted image (T1-weighted FLASH, TR = 12 ms; TE = 5.6 ms; 1 mm³ resolution).

C. PARAMETER SETTING OF EACH MODEL
1) PARAMETER SETTING OF RSF AND LIF IN THE COMPARATIVE EXPERIMENT
The initial contour of the three models is generated through the [x, y] = ginput (n) function, which can select n points from the current graph and return the corresponding coordinate vectors x, y of these points. N points can be positioned by the mouse. We used the mouse to position four points on the target area to generate the initial contour as two rectangles. In the first experiment, the same initial level set contour for the two models were constructed. The segmentation effect and efficiency of the two methods were compared. The adopted parameters for the two models were: in the RSF model, timestep = 0.125, mu = 1, iterNum = 150, lambda1 = 1.0, lambda2 = 1.3, nu = 0.001 × 255 × 255, epsilon = 0.1, sigma = 0.8. In the LIF model, timestep = 0.1, epsilon = 0.2, sigma = 0.6, sigma_phi = 1, iterations = 200.
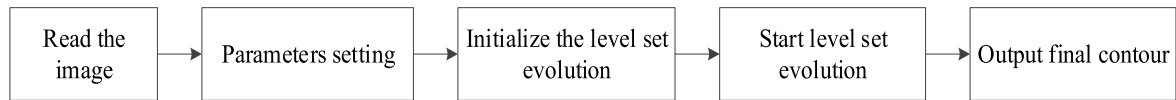
Read the image	→	Parameters setting	→	Initialize the level set evolution	→	Start level set evolution	→	Output final contour

FIGURE 3. The flow chart of the experiment.

Since the MRI image has intensity inhomogeneity, it is difficult to separate the caudate nucleus from the gray matter. Faced with this problem, a small sigma was chosen to make the segmentation results more accurate in the RSF model. In addition, the value of λ_2 was larger than λ_1. This was to avoid a new contour far away from the initial contour and ensure the final contour closer to the target boundary. The profile of $\delta_\varepsilon(\phi)$ was affected by the parameter ε. A larger ε induced a broader profile, which enlarged the capture range, but reduced the accuracy in the final contour. The caudate nucleus that we want to divide is relatively small, so a smaller ε was chosen. The value of v was set to $0.001 \times 255 \times 255$. A larger v further penalizes the length of the contour, but also discouraged the expansion of the contour, to some extent. Thus, this parameter value can be adjusted slightly when needed.

In the LIF model, a small sigma was still chosen to make segmentation results accurate. The value of sigma was selected to be 0.6 based on the images and experience. Besides, the standard deviation sigma_phi of the regularized Gaussian kernel should be chosen between 0.45 and 1 according to experiments. The higher the noise of the image, the larger the sigma_phi should be set. Here, sigma_phi = 1. The size of the Gaussian kernel can be truncated as a 5×5 mask for efficiency.

2) PARAMETER SETTING OF THREE MODELS

In this part, the RSF, LIF and DRLSE models were applied to segment the caudate nucleus, and then the segmentation results were compared and appraised. The optimal experimental parameters were selected for each model as much as possible to get the best segmentation effect. The parameter setting for the DRLSE model was: timestep = 5, mu = 0.2 / timestep, iter_inner = 5, iter_outer = 40, lambda = 5, alpha = −1.5, epsilon = 1.5, sigma = 0.8.

In the DRLSE model, due to the algorithm improvement, a relatively large time step can be used to significantly decrease the number of iterations and improve efficiency. Here, the time step is set to 5. The coefficient of the weighted length term lambda is set to 5. The coefficient of the weighted area term alpha is set to −1.5. It should be noted that alpha should take a negative value when the initial contour is inside the target object and the contour need to expand outward. Conversely, if the initial contour is outside the target object, alpha takes a positive value and the contour contracts inward. For images with weak boundaries, the value of alpha should be relatively small to avoid boundary overflow. Epsilon is usually set to 1.5. For sigma, if the evolution contour is performed from inside to outside, sigma takes a smaller value. On the contrary, sigma takes a larger value.
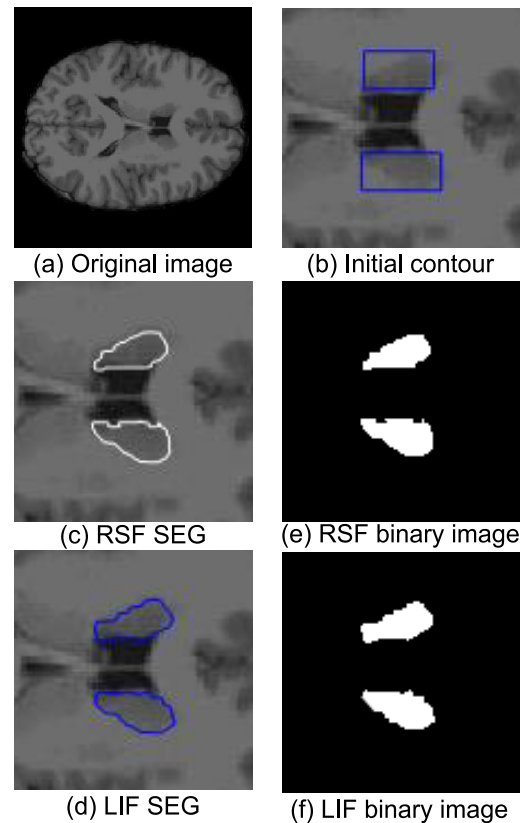

(a) Original image   (b) Initial contour
(c) RSF SEG   (e) RSF binary image
(d) LIF SEG   (f) LIF binary image

FIGURE 4. Segmentation results of RSF model and LIF model.

Minor adjustments are made to the parameter setting in the RSF model. The time step was adjusted to 0.1. In the LIF model, the parameters are not changed.

D. EXPERIMENTAL PLATFORM

All experiments were conducted on a standard PC (Intel Core (TM) i7-8750H, 2.20 GHz processor with 8 GB of RAM). The algorithm was implemented in Matlab r2016a.

IV. RESULTS AND DISCUSSION

A. RESULTS OF SEGEMENTATION OF THE RSF AND LIF MODELS

In this group of experiments, we manually selected the same initial level set function (rectangle initial contour). Through the level set iteration, the segmentation results and iteration time of the two models were obtained.

In Fig. 4, (a) is the original image, (b) to (f) are the zoomed images of the region of interest (ROI). (b) is the same rectangular initial contour image, (c) is the segmentation result of RSF model, (d) is the segmentation result of LIF model, (e) is the binary image of the segmentation result of RSF model.
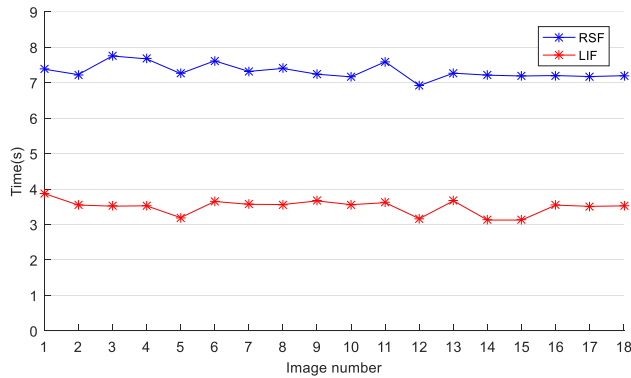
FIGURE 5. Run time of the level set iteration of all experimental images under two models.

(f) is the binary image of the segmentation result of LIF model. From Fig. 4, it is easy to see that for the same segmentation, region (caudate nucleus), the segmentation results of the two models obtained by setting the same initial level set function (rectangular contour) are mostly similar. However, with careful observation, minor differences were found. The segmentation profile of the RSF model was smoother than the LIF model. The RSF model guided the motion of the contour with intensity information in local areas on both sides of the contour, and the arc length term in the evolution equation had a certain smoothing effect of the contour. The LIF model guided the motion of the contour with constraints on the difference between the fitted image constructed from the local image information and the original image. This model removed the traditional regularized term and adopted a Gaussian kernel to regularize the level set function and smooth the contour after each iteration. LIF model can achieve sub-pixel segmentation accuracy. Segmentation contour of the LIF model is rougher than the RSF model.

Figure 5 presents the run time of the level set iteration for all experimental images under the two models. The horizontal axis is the image number and the vertical axis is the run time. The number of iterations in the LIF model is 200, while in the RSF model is 150 according to the effect on segmentation results. It can be seen that although the LIF model had more iterations than RSF model, its running time is still shorter than the RSF model, which confirmed that the LIF model is more efficient than the RSF model as mentioned in the literature by Zhang *et al.* [3].

B. COMPARISIONS WITH THE RSF, LIF, AND DRLSE MODELS

In this section, these three level set models were used to segment the caudate nucleus. The reference image was used as the ground truth (GT) to compare the segmentation results of the models. The manual annotations by an experienced medical practitioner were obtained for reference.

1) RESULTS OF THE SUBJECTIVE EVALUATION

Figure 6 shows the segmentation results of the ground truth, RSF model, LIF model, DRLSE model and their binary
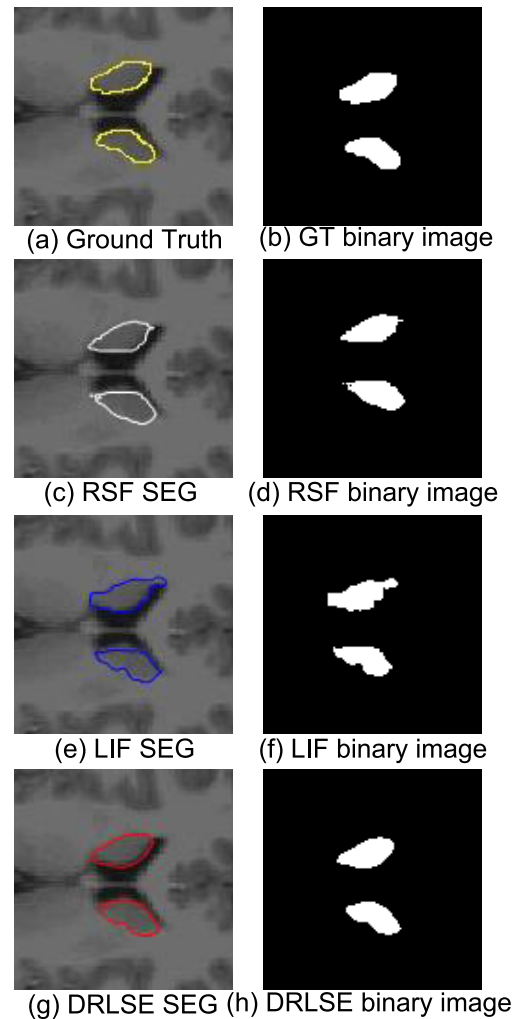

(a) Ground Truth   (b) GT binary image

(c) RSF SEG   (d) RSF binary image

(e) LIF SEG   (f) LIF binary image

(g) DRLSE SEG (h) DRLSE binary image

FIGURE 6. Segmentation results of each model.

images in turn. And (a) to (h) are the zoomed images of the region of interest (ROI). Intuitively, these three methods can segment the caudate nucleus well. It is easy to see from Fig. 6 that the segmentation result of DRLSE model is the closest to the ground truth, and its contour is the smoothest. The DRLSE model used a energy term with double-well potential p_2, which is called a distance regularization term to constrain the level set function to remain stable and smooth throughout the iterative process. After the process of level set evolution was over, the model refound the zero level contour by further level set evolution with alfa = 0, resulting in a smoother segmentation contour. As LIF model can achieve sub-pixel level precision segmentation, it obtains a slightly rough segmentation contour compared with the other two models. However, the phenomenon of under-segmentation or over-segmentation is still observed when the results are compared with the ground truth image in detail. As can be seen in (f), the upper half of the caudate nucleus is over-segmented. Lower half of caudate nucleus in (d) and (f) shows the problem of under-segmentation when compared with the ground truth image. One of the reasons may be that the

TABLE 1. DSC of the three models for all experimental images.

Image number	RSF	LIF	DRLSE
1	0.9322	0.8957	0.9377
2	0.9044	0.8651	0.9546
3	0.9102	0.899	0.9329
4	0.9136	0.9328	0.9288
5	0.8286	0.8386	0.8515
6	0.8551	0.8862	0.8709
7	0.8679	0.8424	0.8931
8	0.8099	0.8347	0.8833
9	0.8993	0.8924	0.9198
10	0.8288	0.8439	0.8914
11	0.7978	0.7578	0.8202
12	0.8038	0.8589	0.9015
13	0.8909	0.9041	0.8895
14	0.863	0.8779	0.8363
15	0.8476	0.8629	0.8749
16	0.8701	0.8456	0.9269
17	0.8326	0.8073	0.8885
18	0.8764	0.9056	0.8971

TABLE 2. JS of the three models for all experimental images.

Image number	RSF	LIF	DRLSE
1	0.8729	0.8111	0.8827
2	0.8255	0.7623	0.9131
3	0.8352	0.8166	0.8743
4	0.841	0.8741	0.8671
5	0.7073	0.722	0.7414
6	0.7469	0.7957	0.7714
7	0.7667	0.7278	0.8069
8	0.6805	0.7163	0.7911
9	0.817	0.8057	0.8515
10	0.7077	0.7299	0.8041
11	0.6637	0.61	0.6953
12	0.6719	0.7527	0.8206
13	0.8033	0.8249	0.8009
14	0.7589	0.7824	0.7187
15	0.7355	0.7589	0.7777
16	0.77	0.7325	0.8638
17	0.7132	0.6768	0.7993
18	0.78	0.8275	0.8133

TABLE 3. Sensitivity of the three models for all experimental images.

Image number	RSF	LIF	DRLSE
1	0.9405	0.9028	0.9107
2	0.8794	0.8197	0.9414
3	0.8724	0.905	0.9184
4	0.8543	0.9009	0.918
5	0.7451	0.7648	0.7678
6	0.7798	0.8528	0.8053
7	0.8058	0.765	0.8175
8	0.7005	0.7477	0.7973
9	0.8503	0.8485	0.8733
10	0.7248	0.7568	0.8391
11	0.6858	0.6405	0.7043
12	0.6911	0.7673	0.8506
13	0.8168	0.8396	0.8446
14	0.7811	0.857	0.7335
15	0.7592	0.7825	0.7802
16	0.7833	0.7661	0.8876
17	0.7445	0.6948	0.8058
18	0.8019	0.8427	0.8291

sensitivity of the algorithm to the initial contour makes the final contour not so close to the target contour. The segmentation accuracy of these models very much depends on the selection of the initial contour. In addition, it is also possible that the parameters of the model were not robust enough. The difference between images leads to the difference of model parameter adaptation. A set of suitable parameters to apply to all experimental images and obtain good segmentation accuracy is required. The third reason could be that the quality of the image is not high enough. The caudate nucleus is small and its boundary is blurred so that it is difficult to accurately segment. Even if experienced medical practitioners segment the caudate nucleus manually, there will be some small errors in the edge.

2) QUANTITATIVE EVALUATION

Quantitative comparison was made between the ground truth and segmentation results using the following metrics [30]: for each segmentation result, the true positive (TP), the true negative (TN), the false positive (FP), and the false negative

(FN) counts were computed. These metrics are defined as:

$$TP = R \cap T; TN = \overline{R \cup T}; FP = R \cap \bar{T}; FN = \bar{R} \cap T \quad (29)$$

where T is the true set representing the ground truth and R is the result set representing the segmentation result. The comparison between the three tested models was made according to the following performance measures, including the Dice Similarity Coefficient (DSC), Jaccard Similarity (JS), Sensitivity (fraction of positives that are correctly detected), and Specificity (fraction of negatives that are correctly detected).

Dice coefficient:

$$DSC = \frac{2 * TP}{(FP + TP) + (TP + FN)} \quad (30)$$

Jaccard similarity:

$$JS = \frac{TP}{FP + TP + FN} \quad (31)$$

Sensitivity:

$$Sens. = \frac{TP}{TP + FN} \quad (32)$$

Specificity:

$$Spec. = \frac{TN}{TN + FP} \quad (33)$$

Both DSC and JS were used to indicate the similarity between the segmentation result and the ground truth. The measure takes a value of 1 in the case of perfect matches amongst the two segmentations, i.e. the closer the value was to 1, the higher the similarity of the segmentation result. When the segmentation results are similar, the JS ratio was more sensitive than DSC. Besides, when the Sensitivity is high, the rate of missed segmentation is low, and when the Specificity is high, the error segmentation rate is low.

The corresponding indicator values of the experimental results are shown in TABLE 1 - 4. From TABLE 1, it can be seen that the DSC values of the three models are primarily above 80%, indicating that these models all can obtain

TABLE 4. Specificity of the three models for all experimental images.

Image number	RSF	LIF	DRLSE
1	0.9995	0.9993	0.9998
2	0.9996	0.9996	0.9998
3	0.9998	0.9995	0.9998
4	0.9999	0.9998	0.9997
5	0.9997	0.9996	0.9998
6	0.9998	0.9996	0.9998
7	0.9998	0.9998	0.9999
8	0.9998	0.9998	1
9	0.9997	0.9996	0.9998
10	0.9998	0.9998	0.9997
11	0.9998	0.9997	0.9999
12	0.9998	0.9999	0.9998
13	0.9999	0.9999	0.9997
14	0.9998	0.9994	0.9999
15	0.9998	0.9998	1
16	0.9999	0.9997	0.9998
17	0.9998	0.9999	1
18	0.9998	0.9999	0.9999

TABLE 5. DSC, JS, sensitivity, and specificity to evaluate image analysis results.

Indicators	RSF	LIF	DRLSE
DSC	0.8691	0.8722	0.9017
JS	0.7704	0.7747	0.8223
Sensitivity	0.7991	0.8156	0.8470
Specificity	0.9998	0.9997	0.9998

good segmentation results. Because JS was more sensitive than DSC for similar segmentation results, its values were generally lower than DSC values.

Finally, we used JS as a standard to exclude two groups with poor segmentation results. Then, we averaged the remaining data creating the results presented in TABLE 5. TABLE 5 shows the performance comparisons between the three models. The results show that the segmentation performance of all three algorithms is good, with the DRLSE model being better than the other two models.

V. CONCLUSION

The aim of this paper was to help the diagnosis and treatment of mental disorders, such as depression, by considering the semi-automated segmentation of the caudate nucleus compared to labor intensive manual segmentation. In view of the advantages of the level set method in segmenting medical images with intensity inhomogeneity, we applied this method to MRI images of the brain to segment the caudate nucleus. The RSF, LIF, and DRLSE models were selected for segmentation. All of the segmentation results were compared with ground truth images, which are manual segmentation images by an experienced medical practitioner. The proposed three methods achieved the average Dice Similarity Coefficient (DSC) values are 0.8691, 0.8722, and 0.9017 and the average Jaccard Similarity (JS) values are 0.7704, 0.7747, and 0.8223, respectively. The results indicate that among the three models, the DRLSE model has the best segmentation ability and each of its indicators have the highest average value. Although the other two methods were lightly worse,

they can still reliably segment the caudate nucleus from images and meet the general segmentation requirements. Hybrid segmentation technqiues needs to be explored when conventional segmentation algorithms fails to achive satisfactory results. In addition, other different metrics requires to be implemented for further evaluation of segmentation results.

In this current study, the main focus was in algorithm development and to deploy the same on an open access data set. The proposed technique was deployed on a limited size public database and is in the process of collecting more relevant data. As a future scope of the work, a larger data pool will be used. Beside this automatic initialization will also be considered to prove the robustness and the efficacy of the proposed technique followed by investigation to look for possibility of any conclusion or statistical analysis produced from the obtained results.

REFERENCES

[1] C. Li, C.-Y. Kao, J. C. Gore, and Z. Ding, "Minimization of region-scalable fitting energy for image segmentation," *IEEE Trans. Image Process.*, vol. 17, no. 10, pp. 1940–1949, Oct. 2008. doi: 10.1109/TIP.2008.2002304.

[2] C. Li, C.-Y. Kao, J. C. Gore, and Z. Ding, "Implicit active contours driven by local binary fitting energy," in *Proc CVPR*, Minneapolis, MN, USA, Jun. 2007, pp. 1–7. doi: 10.1109/CVPR.2007.383014.

[3] K. Zhang, H. Song, and L. Zhang, "Active contours driven by local image fitting energy," *Pattern Recognit.*, vol. 43, no. 4, pp. 1199–1206, Apr. 2010. doi: 10.1016/j.patcog.2009.10.010.

[4] C. Li, C. Xu, C. Gui, and M. D. Fox, "Distance regularized level set evolution and its application to image segmentation," *IEEE Trans. Image Process.*, vol. 19, no. 12, pp. 3243–3254, Dec. 2010. doi: 10.1109/TIP.2010.2069690.

[5] H. S. Bhadauria and M. L. Dewal, "Intracranial hemorrhage detection using spatial fuzzy c-mean and region-based active contour on brain CT imaging," *Signal Image Video Process.*, vol. 8, no. 2, pp. 357–364, Feb. 2014. doi: 10.1007/s11760-012-0298-0.

[6] K. Ding, L. Xiao, and G. Weng, "Active contours driven by region-scalable fitting and optimized Laplacian of Gaussian energy for image segmentation," *Signal Process.*, vol. 134, pp. 224–233, May 2017. doi: 10.1016/j.sigpro.2016.12.021.

[7] L. Wang, Y. Chang, H. Wang, Z. Wu, J. Pu, and X. Yang, "An active contour model based on local fitted images for image segmentation," *Inf. Sci.*, vols. 418–419, pp. 61–73, Dec. 2017. doi: 10.1016/j.ins.2017.06.042.

[8] L. Wang, J. Zhu, M. Sheng, A. Cribb, S. Zhu, and J. Pu, "Simultaneous segmentation and bias field estimation using local fitted images," *Pattern Recognit.*, vol. 74, pp. 145–155, Feb. 2018. doi: 10.1016/j.patcog.2017.08.031.

[9] G. Sethi, B. S. Saini, and D. Singh, "Segmentation of cancerous regions in liver using an edge-based and phase congruent region enhancement method," *Comput. Electr. Eng.*, vol. 53, pp. 244–262, Jul. 2016. doi: 10.1016/j.compeleceng.2015.06.025.

[10] Y. Liu, G. Captur, J. C. Moon, S. Guo, X. Yang, S. Zhang, and C. Li, "Distance regularized two level sets for segmentation of left and right ventricles from cine-MRI," *Magn. Reson. Imag.*, vol. 34, no. 5, pp. 699–706, Jun. 2016. doi: 10.1016/j.mri.2015.12.027.

[11] Y. Zhang, J. Peng, and L. Gang, "Research on the segmentation method of prostate magnetic resonance image based on level set," *Chin. J. Sci. Instrum.*, vol. 38, no. 2, pp. 416–424, Feb. 2017. doi: 10.19650/j.cnki.cjsi.2017.02.020.

[12] A. Gautam, B. Raman, and S. Raghuvanshi, "A hybrid approach for the delineation of brain lesion from CT images," *Biocybern. Biomed. Eng.*, vol. 38, no. 3, pp. 504–518, Apr. 2018. doi: 10.1016/j.bbe.2018.04.003.

[13] J. Wu, T. R. Mazur, S. Ruan, C. Lian, N. Daniel, H. Lashmett, L. Ochoa, I. Zoberi, M. A. Anastasio, H. M. Gach, S. Mutic, M. Thomas, and H. Li, "A deep Boltzmann machine-driven level set method for heart motion tracking using cine MRI images," *Med. Image Anal.*, vol. 47, pp. 68–80, Jul. 2018. doi: 10.1016/j.media.2018.03.015.

[14] L. Hussain, "Detecting epileptic seizure with different feature extracting strategies using robust machine learning classification techniques by applying advance parameter optimization approach," *Cogn. Neurodyn.*, vol. 12, no. 3, pp. 271–294, Jun. 2018. doi: 10.1007/s11571-018-9477-1.

[15] G.-S. Yi, J. Wang, B. Deng, and X.-L. Wei, "Complexity of resting-state EEG activity in the patients with early-stage Parkinson's disease," *Cognit. Neurodyn.*, vol. 11, no. 2, pp. 147–160, Apr. 2017. doi: 10.1007/s11571-016-9415-z.

[16] S. D. S. Al-shaikhli, M. Y. Yang, and B. Rosenhahn, "Alzheimer's disease detection via automatic 3D caudate nucleus segmentation using coupled dictionary learning with level set formulation," *Comput. Methods Programs Biomed.*, vol. 137, pp. 329–339, Dec. 2016. doi: 10.1016/j.cmpb.2016.09.007.

[17] K.-I. Amemori, S. Amemori, D. J. Gibson, and A. M. Graybiel, "Striatal microstimulation induces persistent and repetitive negative decision-making predicted by striatal beta-band oscillation," *Neuron*, vol. 99, no. 4, pp. 829–841, Aug. 2018. doi: 10.1016/j.neuron.2018.07.022.

[18] Z. Tian, N. Dey, A. S. Ashour, P. McCauley, and F. Shi, "Morphological segmenting and neighborhood pixel-based locality preserving projection on brain fMRI dataset for semantic feature extraction: An affective computing study," *Neural Comput. Appl.*, vol. 30, no. 12, pp. 3733–3748, Dec. 2018. doi: 10.1007/s00521-017-2955-2.

[19] Z. Karimaghaloo, D. L. Arnold, and T. Arbel, "Adaptive multi-level conditional random fields for detection and segmentation of small enhanced pathology in medical images," *Med. Image Anal.*, vol. 27, pp. 17–30, Jan. 2016. doi: 10.1016/j.media.2015.06.004.

[20] E. Abdel-Maksoud, M. Elmogy, and R. Al-Awadi, "Brain tumor segmentation based on a hybrid clustering technique," *Egyptian Inform. J.*, vol. 16, no. 1, pp. 71–81, Mar. 2015. doi: 10.1016/j.eij.2015.01.003.

[21] S. De, S. Bhattacharyya, and P. Dutta, "Automatic magnetic resonance image segmentation by fuzzy intercluster hostility index based genetic algorithm: An application," *Appl. Soft Comput.*, vol. 47, pp. 669–683, Oct. 2016. doi: 10.1016/j.asoc.2016.05.042.

[22] S. Abdel-Khalek, A. B. Ishak, O. A. Omer, and A.-S. F. Obada, "A two-dimensional image segmentation method based on genetic algorithm and entropy," *Optik*, vol. 131, pp. 414–422, Feb. 2017. doi: 10.1016/j.ijleo.2016.11.039.

[23] J. Minnema, M. van Eijnatten, W. Kouw, F. Diblen, A. Mendrik, and J. Wolff, "CT image segmentation of bone for medical additive manufacturing using a convolutional neural network," *Comput. Biol. Med.*, vol. 103, pp. 130–139, Dec. 2018. doi: 10.1016/j.compbiomed.2018.10.012.

[24] B. D. Barkana, I. Saricicek, and B. Yildirim, "Performance analysis of descriptive statistical features in retinal vessel segmentation via fuzzy logic, ANN, SVM, and classifier fusion," *Knowl.-Based Syst.*, vol. 118, pp. 165–176, Feb. 2017. doi: 10.1016/j.knosys.2016.11.022.

[25] S. Osher and J. A. Sethian, "Fronts propagating with curvature-dependent speed: Algorithms based on Hamilton-Jacobi formulations," *J. Comput. Phys.*, vol. 79, no. 1, pp. 12–49, 1988. doi: 10.1016/0021-9991(88)90002-2.

[26] M. Kass, A. Witkin, and D. Terzopoulos, "Snakes: Active contour models," *Int. J. Comput. Vis.*, vol. 1, no. 4, pp. 321–331, 1988. doi: 10.1007/BF00133570.

[27] C. Xu and J. L. Prince, "Snakes, shapes, and gradient vector flow," *IEEE Trans. Image Process.*, vol. 7, no. 3, pp. 359–369, Mar. 1998. doi: 10.1109/83.661186.

[28] T. F. Chan and L. A. Vese, "Active contours without edges," *IEEE Trans. Image Process.*, vol. 10, no. 2, pp. 266–277, Feb. 2001. doi: 10.1109/83.902291.

[29] K. J. Duncan, C. Pattamadilok, I. Knierim, and J. T. Devlin, "Consistency and variability in functional localisers," *NeuroImage*, vol. 46, no. 4, pp. 1018–1026, Jul. 2009. doi: 10.1016/j.neuroimage.2009.03.014.

[30] J. Jiang, Y. Wu, M. Huang, W. Yang, W. Chen, and Q. Feng, "3D brain tumor segmentation in multimodal MR images based on learning population- and patient-specific feature sets," *Comput. Med. Imag. Graph.*, vol. 37, nos. 7–8, pp. 512–521, Oct./Dec. 2013. doi: 10.1016/j.compmedimag.2013.05.007.

YATING CHEN received the B.S. degree in biomedical engineering from Zhejiang Sci–Tech University, China, in 2017. She is currently pursuing the master's degree in biomedical engineering with the College of Information and Engineering and the First Affiliated Hospital of Wenzhou Medical University, China. Her research interest includes data mining, adaptive neuro networks, medical image analysis, deep learning for medical images, and fMRI image semantic retrieval.

GAOXIANG CHEN received the B.S. degree in chemical engineering from the Xi'an University of Science and Technology, China, in 2018. He is currently pursuing the master's degree in biomedical engineering with the College of Information and Engineering and the First Affiliated Hospital of Wenzhou Medical University, China. His research interest includes machine learning, MRI imaging technologies, 3-D reconstruction of medical dataset, and random forest algorithm.
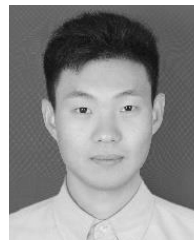
YU WANG received the B.S. degree in biomedical engineering from Taishan Medical University, China, in 2016. He is currently pursuing the master's degree in biomedical engineering with the College of Information and Engineering and the First Affiliated Hospital of Wenzhou Medical University, China. His research interest includes medical image mining, microscopic image analysis, and deep neural networks. He has published five articles in journals.

NILANJAN DEY was born in Kolkata, India, in 1984. He received the B.Tech. and M.Tech. degrees in information technology from the West Bengal University of Technology, in 2005 and 2011, respectively, and the Ph.D. degree in digital image processing from Jadavpur University, India, in 2015. In 2011, he was appointed as an Assistant Professor with the Department of Information Technology, JIS College of Engineering, Kalyani, India, followed by the Bengal College of Engineering College, Durgapur, India, in 2014. He is currently an Assistant Professor with the Department of Information Technology, Techno India College of Technology, India. His research interests include signal processing, machine learning, and information security. He is also an Associate Editor of IEEE ACCESS, the Editor-in-Chief of the *International Journal of Ambient Computing and Intelligence*, and a Series co-editor of *Springer Tracts of Nature-Inspired Computing* (STNIC).

R. SIMON SHERRATT (M'97–SM'02–F'12) received the B.Eng. degree in electronic systems and control engineering from Sheffield City Polytechnic, U.K., in 1992, and the M.Sc. degree in data telecommunications and the Ph.D. degree in video signal processing from the University of Salford, U.K., in 1994 and 1996, respectively. In 1996, he has appointed as a Lecturer in electronic engineering with the University of Reading, where he is currently a Professor of biosensors. His research interests include signal processing and communications in consumer devices focusing on wearable devices and healthcare. He was a recipient of the first place IEEE Chester Sall Memorial Award, in 2006, and second place, in 2016. He is also a Reviewer for the IEEE Sensors Journal and the Editor-in-Chief of the IEEE Transactions on Consumer Electronics.

FUQIAN SHI (M'08–SM'10) received the Ph.D. degree in engineering from the College of Computer Science and Technology, Zhejiang University. He was a Visiting Associate Professor with the Department of Industrial Engineering and Management System, University of Central Florida, Orlando, FL, USA, from 2012 to 2014. He is currently an Associate Professor with the College of Information and Engineering and the First Affiliated Hospital of Wenzhou Medical University. He serves more than 30 committee board memberships of international conferences. He has published more than 80 journal articles and conference proceedings. His research interests include fuzzy inference system, artificial neuro networks, and biomechanical engineering. He also serves as an Associate Editor of the *International Journal of Ambient Computing and Intelligence* (IJACI), the *International Journal of Rough Sets and Data Analysis* (IJRSDA), and a Special Issue Editor of fuzzy engineering and intelligent transportation in Information: *An International Interdisciplinary Journal*.

● ● ●